

# A Comprehensive Case Study of Macrosegregation in a Steel Ingot

E.J. Pickering<sup>1</sup>, C. Chesman<sup>2</sup>, S.S. Al-Bermani<sup>2</sup>, M. Holland<sup>3</sup>,  
P. Davies<sup>2</sup> and J. Talamantes-Silva<sup>2</sup>

<sup>1</sup> Corresponding author. Department of Materials Science and Metallurgy, University of Cambridge, 27 Charles Babbage Road, Cambridge, CB3 0FS, UK.  
Email: ejp57@cam.ac.uk. Tel: +44 (0) 1223334434.

<sup>2</sup> Sheffield Forgemasters International Ltd., Brightside Lane, Sheffield, S9 2RW, UK.

<sup>3</sup> Geotek Ltd., 4 Sopwith Way, Daventry, NN11 8PB, UK.

## Abstract

A case study is presented that examines the macrosegregation and grain structure present in a 12 ton steel ingot, which was cast for experimental purposes. Details of the casting procedure were well documented and the resulting ingot was characterised using a number of techniques that measured chemical segregation, shrinkage and porosity. The formation of the porosity and segregation patterns are discussed in reference to the particular grain structure observed in the ingot. It is hoped that this case study can be used as a tool for the validation of future macromodels.

## 1 Introduction

The segregation of alloying elements over large distances during the casting of ingots continues to be associated with the manufacture of large steel components, despite many decades of research. The heterogeneities that can arise from this macrosegregation, shown in Fig. 1, are impossible to remove using any practical heat treatment and can have a detrimental effect on mechanical properties (see, for instance, the literature for A-segregation in SA508 Grade 3 pressure-vessel steel [1, 2, 3, 4]). Our understanding of the underlying causes and mechanisms of macrosegregation has progressed dramatically since the earliest investigations of ingot heterogeneity, but predictive capabilities are still limited [5, 6, 7]. Computing power is arguably the most prominent restraint on the effectiveness of current macromodels, but there is also a definite lack of suitable case studies against which model results can be compared.

In this paper, we present a comprehensive experimental evaluation of macrosegregation in a steel ingot. In order to create a study that can act as a suitable validation tool for macromodellers, as much information as possible has been collected about the casting apparatus and procedure, as well as the resulting ingot characteristics. For instance, temperature distributions during casting were measured using thermocouples and a thermal imaging camera, ingot

and mould dimensions were measured using lasers, and chemistry distributions were mapped using macro-scale X-ray fluorescence spectroscopy (XRF). The application of macro-scale XRF here represents a significant improvement over previous methods used for chemical analyses of steel ingots, which have usually involved periodic trepanning of material and, on occasion, questionable interpolation of such data to produce contour maps [1, 9, 10]. Here, a cross section of the ingot is mapped in its entirety - never before has a steel ingot been mapped for chemistry in such detail. Indeed, to the author’s knowledge no metallic specimen has ever been mapped so completely on a scale so large [11].

A 12 ton steel ingot with high C, Si and Cr additions was used as the case study [12]. In this document, the aspect ratios of the ingot and casting apparatus have been changed due to their commercial sensitivity, and their dimensions have been removed. The flutes on the outside of the ingot have also been removed, giving it a smooth surface profile.

## 2 Experimental

### 2.1 Ingot Selection

The composition of the ingot cast, which was measured at the point of pouring, is given in Table 1. This particular steel composition was chosen because its high C and Si levels were predicted to deliver particularly prominent macrosegregation (C and Si strongly enrich the interdendritic liquid and cause its density to decrease significantly, hence they promote advection of alloying elements). This allowed for the ingot size to be kept small, eliminating practical issues associated with the analysis of a larger ingot - larger ingots would usually be preferred for such studies, as their longer solidification times naturally generate more macrosegregation.

### 2.2 Casting Apparatus and Procedure

The full casting set up is shown in Fig. 2; each component labelled is described in Table 2. Appropriate physical properties of the materials used are given in Appendix 1. A FARO Focus3D S laser scanner was used to verify the dimensions of these components and produce three-dimensional CAD (computer-aided design) models of the components for reference.

Molten steel for the ingot was produced by heating scrap material in an electric arc furnace. The steel produced was then teemed into a ladle and vacuum-arc degassed. The ladle contained  $\approx 100$  tons of steel at a temperature above  $1500^\circ\text{C}$  at the end of degassing. The oxygen content of the steel was measured to be less than 0.001 wt% at this stage. The ingot investigated was poured approximately 50 min after the end of degassing; it is therefore probable that the melt was below  $1500^\circ\text{C}$  at the time of casting. The mould was filled approximately to the top of the insulating tiles. A flux comprising various oxides was added to the surface of the melt to capture any floating inclusions. An anti-piping compound was added to the top of the ingot after pouring, which kept the head of the ingot hot. Lifting hooks were integrated into the top of the head to allow for the ingot to be extracted at the end of solidification (this extraction process is referred to as ‘stripping’). The temperature of the outside of the mould was monitored continuously throughout the casting procedure using thermocouples and a thermal imaging camera. The thermal imaging camera used was a FLIR ThermoCAM SC640 instrument, which was calibrated up to  $2000^\circ\text{C}$ . It was used with a target emissivity value of 0.8 and in high-temperature mode, which meant it was only capable of accurately measuring temperatures above  $200^\circ\text{C}$ . K-type (chromel-alumel) thermocouples were located as shown in

Fig. 3. TC1-4 were placed in the top of the mould between the mould and insulating tiles (labelled with superscript ‘\*’). TC1 and TC3 were held in place by friction (labelled with superscript ‘f’), whilst TC2 and TC4 were cemented. TC5-14 were placed in 10 mm holes drilled into the mould at regularly-spaced intervals, and were held in place with cement. TC15 and TC16 were cemented in place in gaps between the cover plate and the base plate. Temperature measurements from each thermocouple were made every second from steel pouring until the ingot was removed from the mould. Thermal images of the ingot were also taken immediately after removal from the mould.

### 2.3 Post-Casting Analysis

The ingot was removed from the mould after  $\approx 7$  hours (25000 s). Temperature measurements were made at this stage using the thermal-imaging camera, and dimensional measurements were also made using the laser scanner. The ingot was then transferred for to a furnace for the heat treatment given in Table 3. This heat treatment was designed to minimise changes to the as-cast structure of the ingot whilst providing adequate stress relief. Following heat treatment, the ingot was sectioned to examine the faces labelled A-D in Fig. 4.

Faces A, B, C and D were metallographically prepared to a near-mirror finish. Face A was then subject to chemical mapping using an automated macro-scale XRF technique, the use of which was examined in another article [13]. An Olympus Innov-X Delta Dynamic hand held XRF analyser was employed, with robotics designed and constructed by Geotek Ltd [14]. The beam energy used was 40 kV, with a beam of current  $52 \mu\text{A}$ . The step size used was 5 mm in both orthogonal directions of movement, and the dwell time was 10 s. Faces A, B, C and D were then all macroetched in 10% aqueous nitric acid. A radial slice of Face C was subsequently sectioned, metallographically prepared and etched in 2% nital to reveal variations in microstructure. Optical micrographs were taken using a stereo microscope, whilst secondary-electron imaging and energy-dispersive X-ray (EDX) analyses were carried out with a CamScan MX2600 FEG-SEM. Optical-emission spectrometry (OES) measurements were made on a selection of trepanned samples to demonstrate the co-segregation of alloying elements and impurities.

## 3 Results

### 3.1 Thermal Data

The temperature profiles for a selection of thermocouples are shown in Fig. 5. There was good agreement between the two sets of thermocouples placed down the outside of the mould (TC5-9 and TC10-14). Thermal images of the mould after 2500, 10000 and 25000 s are shown in Fig. 6a-c. A comparison of these results to the thermocouple results suggests (assuming the thermocouple results are accurate) that the emissivity used for calibration of the thermal imaging camera (0.8) was too low - the temperatures measured by the thermal imaging camera were consistently higher than the thermocouple readings (the discrepancy rose with temperature, and was  $\approx 25^\circ\text{C}$  at  $540^\circ\text{C}$ ), and should only be used qualitatively.

A thermal image of the ingot taken immediately following its removal from the mould is shown in Fig.6d. An approximate temperature variation from  $\approx 850^\circ\text{C}$  at base of the head (just below the tiles, at the top of the chill) to  $\approx 500^\circ\text{C}$  at the very bottom of the ingot is

observed. It should be noted, however, that once again an emissivity of 0.8 was used for the acquisition of this data, which could have introduced a systematic error as described above.

### 3.2 Dimensional Data

The dimensions of the ingot were measured using laser scanning immediately after its removal from the mould, as well as after cooling to room temperature ( $\approx 15^\circ\text{C}$ ) following stress relief. The mould dimensions were also measured at room temperature, as well as shortly after stripping, when the inside and outside temperatures of the mould were  $\approx 480^\circ\text{C}$  and  $\approx 460^\circ\text{C}$ , respectively. Using this data, Table 4 gives an indication of the shrinkage of the components over these temperature ranges. The shrinkage gap when both ingot and mould were cold is also given, as is the gap when both were hot (the ingot at its stripping temperature and the mould  $\approx 470^\circ\text{C}$ ). It is hoped that this data can be used to help estimate the evolution of a shrinkage gap during solidification, although no measurements were taken when the metal was liquid.

### 3.3 Porosity

Fig. 8 shows the porosity observed in Face A of the ingot. Very little porosity is observed in the head and the base of the ingot, but it is found in the mid-section, where it forms chevrons that branch out from the middle to the base of the ingot. Smaller strings of porosity were also observed to lie along channels with near-vertical alignment, further from the centre of the ingot, and extended further towards the ingot top. These strings were intersected by Face B nearer the head of the ingot, and were approximately circular in cross section. Face D showed no porosity that was observable by eye [12].

### 3.4 Macrosegregation Measurements

The results of the macro-scale XRF measurements are presented in Fig. 9 for Cr and Mo. Each map comprises over 71,000 datapoints. The presence of A-segregate strings, as well as top-bottom and centreline segregation patterns, is clearly demonstrated. A cone of negative segregation at the base of the ingot is also observed, and it is evident that the material surrounding A-segregates is depleted in solute relative to the edges of the ingot. Maps for Mn and Ni are not presented here due to the excessive noise found in their results - this can be attributed to their relatively low concentrations and the intensity of the background around their  $K_\alpha$  peaks (the background was essential zero at the Mo  $K_\alpha$  energy) [13]. A comparison of the results of chemistry measurements with porosity measurements demonstrated clearly that the vertical strings of porosity (not the chevrons) observed in the ingot were associated with A-segregate channels [12].

The results of OES measurements made on material trepanned from the ingot, including highly enriched material from the very top, are shown in Fig. 10. The concentration of all the alloying elements, apart from Cr, are plotted against Mo. It is clear that C, Si, P, S, Mn, Sn and V all cosegregate with Mo, with C and S segregating most strongly, as might have been expected, given their standard liquid-solid partition coefficients [15]). No consistent trend is observed for Ni, Al and Cu; their near-unity partition coefficients, in combination with their relative scarcities, are likely to have contributed to this.

### 3.5 Macrostructure

The results of macroetching revealed the grain structure of the ingot to be predominantly equiaxed. A columnar grain morphology was observed around the very edge of the ingot in the chill zone and at the base, but these grains only protruded into the casting for  $\approx 100$ -150 mm, Fig. 11a. Fig. 11b shows the grain structure present in half of Face B. The grain boundaries of the grains have etched to give a lighter colour than the grain interiors. The shape of most of the grains away from the outside of the ingot appears to be relatively equiaxed, although there is an indication of some grain elongation along the radial direction. Note that de-smutting during etching has led to streaks of contrast radially and vertically in the image - this is not to be confused with any macrosegregation effect. Indeed, images of the other macroetched slices are not reproduced here not only because the fine scale of the grains (and A-segregates) would be difficult to observe in macroshots if they were printed on a small scale, but also because the same streaking was introduced by the etching procedure used, and the author was keen to avoid confusion generated by this [12]. The results of macroetching the ingot slices did not appear to reveal any consistent large-scale variations radially or along the axis of the ingot (in contrast to the chemistry measurements). At the base of the ingot above the columnar zone, the grain structure was not readily perceptible at the macroscopic scale.

### 3.6 Microstructure

Microstructural analyses were performed on a radial strip of material taken from Face C, Fig. 4, which was sectioned into 12 pieces. The variation in dendritic structure along this strip is shown in Fig. 12, looking along the axial direction. Estimates were made of the secondary-arm spacings in each of the 12 samples by measuring fragments of the dendrites discernible in these micrographs, see Table 5. There is significant uncertainty associated with these results, not least because of sectioning effects, but it is evident that the spacings rapidly increase moving away from the wall (where they are  $<100\mu\text{m}$ ) and soon plateau around  $300\mu\text{m}$ . By over-etching the samples, the grains generated by these dendrites could be observed as in Fig. 11b. The result of outlining these grains by hand is presented in Fig. 13. Despite the subjectivity of this assessment, when taken together with the other macrostructure and microstructure results, they present clear evidence that the grains in most of the ingot were not consistently orientated or significantly elongated. Viewing tangentially, the only samples in which differences were found (when compared to viewing axially) were Samples 1-3, in which a columnar structure was found, Figs. 14a-c. These columnar dendrites ceased in Sample 3 (after  $\approx 100$  mm), and the near-equiaxed morphology predominated from then onwards. The chevrons of porosity present in the ingot appeared to follow the boundaries between equiaxed grains.

Analysis of the structure of the ingot at its base (above the columnar zone, examined by sectioning Face D), again revealed a near-equiaxed structure, with grain size and distribution similar to Samples 10-12 in Fig. 13, see Fig. 14d. The boundaries of these grains were not as easily discernable as for the material in Face C.

### 3.7 A-segregates

A-segregate channels were visible in Faces A-C after etching as channels of material rich in a silver-coloured phase not attacked by the etchant, Fig. 15, but the contrast was such that they were not always clearly distinguishable in macroshots of the slices. Channels were found in Face A at the locations measured using XRF, and were all  $\approx 5$  mm in diameter. The ‘silvery’

phase appeared to have formed in interdendritic regions, Fig. 15b. Flecks of this ‘silvery’ phase were found throughout the ingot in interdendritic regions, but in lower concentration. They were relatively sparse at the base of the ingot and increased in number towards the enriched top and centre (see the radial variation in Fig. 12).

Closer examination of the ‘silvery’ phase under the SEM revealed it to comprise many fine Cr-rich carbides, Figs. 16b-c. JMatPro and ThermoCalc calculations suggest that these carbides are likely to be  $M_7C_3$ ,  $M_3C_2$  or  $M_{23}C_6$  type, but this was not confirmed experimentally [17, 18].

## 4 Discussion

It is evident that the ingot cast, sectioned and analysed here displays all of the classical macrosegregation features that might be expected in a large steel ingot, apart from V-segregation. Nevertheless, their presence (or absence) is not explained easily given the context of the results presented, and some careful deliberation is needed.

The results of XRF suggest there was substantial advection of enriched interdendritic liquid during casting. Cr and Mo have evidently enriched the interdendritic liquid and depleted the solid, and the results of OES suggest that this has also have been the case for C, Si, Ni, Mn, P and S. The enrichment of the interdendritic liquid appears to have caused its density to decrease, leading to A-segregation and enrichment at the top of the ingot. It is likely that the negatively-segregated cone measured at the base of the ingot was formed by the sedimentation of depleted solid, although the fluid-flow pattern in the ingot may have had an effect also (as discussed below).

In terms of grain structure, solidification appears to have started through columnar growth of fine dendrites from the outer skin of the ingot (angled due to non-vertical isotherms), and then transitioned quite rapidly into a near-equiaxed mode of freezing with coarser dendrites as the cooling rate dropped (near-equiaxed because sometimes the grains tended to be elongated slightly along the growth direction). A decrease in the temperature gradient ahead of the solidification interface is likely to have been the cause of this columnar-to-equiaxed transition [16]. The presence of an equiaxed zone is of interest because it is difficult to see how A-segregates could have formed in an equiaxed network, particularly segregates that are so straight and long. Of course, there is no reason why A-segregates cannot form in equiaxed structures, and they have been observed in such regions historically [19], but it must be the case that the networks in which they do form are stationary and stable. It is not immediately clear how this could have been the case in the ingot studied, although the stability of an equiaxed network moving away from the sides may have been facilitated naturally by the shape of the isotherms, Fig. 17.

What remains unexplained, however, is why no A-segregation was observed at the centre and base of the ingot. Historically, these areas have been found to be free of A-segregates [8, 20], in agreement with the findings of this study, but it is not immediately clear why this should be the case. In order for A-segregate channels to form, enriched interdendritic liquid must move from colder to warmer parts of the casting, i.e., the fluid must cross isotherms [21]. If it is assumed the enriched fluid is moving with a near-vertical velocity, then channel formation should be more difficult at the sides of the ingot, where the isotherms are oriented near-vertically - in the

limiting case of perfectly vertical isotherms and fluid velocities, the fluid would need to move infinitely fast to cross isotherms. By this reasoning, the expected A-segregate pattern should essentially be the inverse of what is observed. A possible reconciliation is that, although the thermal conditions are more favourable for channel formation at the base and centre of the casting, there is kinetic inhibition of this in these regions.

There are a number of possible mechanisms for this inhibition; one is likely to have been the pattern of fluid flow in the ingot, Fig. 18. It is probable that this was in a downwards direction in the centre of the casting, such that it complemented upwards flow through A-segregate channels in the mushy zone. Any downwards flow in the bulk liquid would have suppressed channel formation at the base and centre of the ingot, and may also help explain the shape of the negatively-segregated cone. Note that the flow through the channels would likely have been vigorous [22, 23], and the flow in the bulk slower. It is possible that the bulk liquid is stratified in such large ingots, and falls steadily as less dense liquid is added to the top of the liquid pool.

Channel formation may also have been impeded in other ways: if the negative cone had been formed by grain sedimentation, then this would have made the shearing off or blocking of channels more likely. Decreased local permeability could also have arisen through increased compaction of the sedimenting solid grains, perhaps because they became more globular whilst suspended in the liquid (Fig. 14d did not show any sign of more globular grains, but it was taken from Face D, which was located at the very base of the cone). Also, the flushing out of enriched liquid and its replacement by bulk liquid (relatively solute poor) is likely to have decrease the density change associated with the enrichment of the interdendritic liquid, and hence made channel formation less likely (this argument cannot be made above the cone). In the central zone, shrinkage stresses could have caused significant movement of the network (and, indeed, voiding of it too), making channel formation more difficult.

A-segregates appear to have formed very soon after the end of the columnar zone. Their onset corresponds to a loss of chemical homogeneity in the solid, which is significantly depleted in solute by their formation. Before the start of A-segregation, there will have been significantly less top-bottom segregation in the ingot, and no macrosegregation would have been visible at all if only the material before this point was assessed (i.e., the outer columnar skin). The XRF measurements indicate that the material within A-segregate channels was not enriched to a consistent level across the whole ingot. This result may have been due to sectioning effects and the particular placement of each XRF measurement, but the change in the concentration of the remaining liquid at each stage should have affected the concentration of the corresponding enriched interdendritic fluid.

The porosity found in the ingot is also a compelling topic for discussion. First, it is evident that the hot top anti-piping compound has worked well, eliminating a pipe and insulating the head of the ingot such that the last liquid to solidify was at the very top (based on the level of enrichment found here). No porosity is observed in the head of the ingot apart from in A-segregate channels, indicating excellent feeding as the isotherms moved towards the top of the ingot. The bulk of the porosity present is in the ingot mid section, and appears to start directly above the negative cone. This suggests that completed feeding was difficult at this stage, and this might be attributed to the acceleration of the isotherms at this time (both in terms of direction and speed), Fig. 19. The length of the fissures suggests that they formed late on across a sizeable equiaxed network, which would have been difficult to feed. It is worth

noting that if these pores had been fed by enriched liquid, they would have resembled something akin to inverted V-segregates. Their chevron shape appears to have originated from the shape of the negative cone, but could also have been influenced by shrinkage stresses and the shapes of isotherms (the chevrons appear to have formed perpendicular to isotherms).

Much of the discussion above has been quite speculative, but there are good reasons for this. Prediction of the macrosegregation patterns in a large ingot using macromodels is a formidable challenge, and results are often not particularly reliable or informative [7]. A critical issue is that A-segregates need to be resolved by calculations, because without fluid flow through such channels in the mush, predictions of macrosegregation and fluid-flow patterns *cannot* be made. To date, no macromodel has been produced for large ingots that resolves A-segregates adequately - to do so would require a millimetre-sized mesh or smaller.

#### 4.1 XRF as an Assessment Technique

The results of this study have further demonstrated that XRF is a very effective tool for the measurement of macrosegregation and the detection of macrosegregation features. Indeed, after seeing the results of macroetching like those in Fig. 11, one might even argue that it is superior to macroetching in terms of its ability to detect segregation. The results of macroetching are dependent on the microstructure, and microstructures may sometimes appear insensitive to chemistry given a particular heat treatment. For example, if an alloy is very hardenable, then it may form martensite or bainite throughout a large thickness regardless of size or variations in chemistry, and it may appear relatively homogeneous when macroetched. Furthermore, macroetching cannot reliably inform the user of whether the material is enriched or depleted in solute, as they are not necessarily consistent in terms of appearance (i.e., enriched material might usually be expected to etch darker, but this was not found here).

### 5 Summary and Conclusions

1. The results presented here form a complete and detailed case study of the solidification of a steel ingot, which was cast under conditions that were well documented and are representative of a typical production route. It is hoped that this study provides macromodellers with a valuable validation tool.
2. Macro-scale XRF revealed that there had been marked macroscopic chemical segregation during the solidification of the ingot. A-segregate channels were observed and a negatively-segregated cone was also present. There was significant top-bottom segregation. It was evident that microsegregation had enriched the interdendritic liquid such that its density has decreased, causing it to rise in the casting.
3. Examination of the bulk grain structure of ingot revealed that it had solidified in a near-equiaxed manner, with dendritic grains that were usually randomly oriented and not significantly elongated. The presence of A-segregates within a network of grains of this morphology is not easily explained, although possible explanations have been presented. The pattern of fluid flow in the mushy and bulk-liquid zones is likely to have played a significant role. Further discussion and clarification is required.
4. In many respects, XRF represents a superior method for measuring macrosegregation (and determining the location of macrosegregation features) than macroetching.

5. Future work should include comparison of the results with simulations of ingot casting. These should not only be complex macromodels, but also more simple models that predict characteristics like shrinkage gaps and porosity.

## 6 Acknowledgements

This work was undertaken as part of a project sponsored by Rolls-Royce Power Nuclear plc in collaboration with Sheffield Forgemasters International. The corresponding author would like to thank Prof. Grae Worster and Prof. Christoph Beckermann for very helpful discussions. Requests for access to the underlying research data should be directed to the corresponding author, and will be considered against commercial interests and data protection.

## References

- [1] C. Maidorn and B. Blind: *Nucl. Eng. Des.*, 1985, vol. 84, pp. 285–296.
- [2] S.G. Druce: AERE Report R9581. September 1979.
- [3] M. Bethmont, J-M. Frund, B. Houssin, and P. Soulat: *Effects of Radiation on Materials: 17th Int. Symp.*, ASTM STP 1270, 1996, pp. 320–330.
- [4] P. Soulat, B. Houssin, P. Bocquet, and M. Bethmont: *Radiation Embrittlement of Nuclear Reactor Pressure Vessel Steels: An International Review*, ASTM STP 1170, 1993, pp. 249–265.
- [5] C. Beckermann: *Int. Mater. Rev.*, 2002, vol. 47, pp. 243–261.
- [6] V.R. Voller and F. Porte-Agel: *J. Comput. Phys.*, 2002, vol. 179, pp. 698–703.
- [7] E.J. Pickering: *ISIJ*, 2013, vol. 53, pp. 935–949.
- [8] M.C. Flemings: *Solidification Processing*. McGraw-Hill, January 1974.
- [9] R. Tanzer, W. Schutzenhofer, G. Reiter, H.P. Fauland, L. Konozy, A. Ishmurzin, M. Wu, and A. Ludwig: *Metall. Mater. Trans. B*, 2009, vol. 40B, pp. 305–311.
- [10] H. Combeau, M. Zaloznik, S. Hans, and P.E. Richey: *Metall. Mater. Trans. B*, 2009, vol. 40B, pp. 289–304.
- [11] J.S. Krafcik and J.A. Brooks. *Developments in Materials Characterization Technologies*, ASM International, 1996, pp. 111–118.
- [12] E.J. Pickering, *Ph.D. thesis*, University of Cambridge, 2014.
- [13] E.J. Pickering and M. Holland: *Ironmak. Steelmak.*, 2014, vol. 41, pp. 493–499.
- [14] Geotek Ltd, Daventry, UK, <http://www.geotek.co.uk/>.
- [15] T.B. Massalski, H. Okamoto, P.R. Subramanian, and L. Kacprzak, editors: *Binary Alloy Phase Diagrams*. ASM International, 1990.
- [16] W. Kurz and D.J. Fisher: *Fundamentals of Solidification*. 3rd ed., Trans Tech Publications LTD, Switzerland, 1986.

- [17] JMatPro software, version 6.2.1, <http://www.sentesoftware.co.uk/jmatpro.aspx>.
- [18] ThermoCalc software, version 4.0, database TCFE6, <http://www.thermocalc.com/start/>.
- [19] M. Durand-Charre: *Microstructure of Steels and Cast Irons*. Springer, 2004.
- [20] Heterogeneity Sub-Committee of the British Iron and Steel Institute: *J. Iron Steel I.*, 1926, vol. 113, pp. 39–151.
- [21] R. Mehrabian, M. Keane, and M.C. Flemings: *Metall. Trans.*, 1970, vol.1, pp. 3238–3241.
- [22] A. Sample and A. Hellawell: *Metall. Trans. B*, 1982, vol. 13B, pp. 495–501.
- [23] S. Karagadde, L. Yuan, N. Shevchenko, S. Eckert, and P.D. Lee: *Acta Materialia*, 2014, vol. 79, pp. 168–180, videos 1–4 in supplementary material.
- [24] E.J. Pickering, S.S. Al-Bermani, and J. Talamantes-Silva. *Mater. Sci. Tech.*, in press.

## 7 Figures and Tables

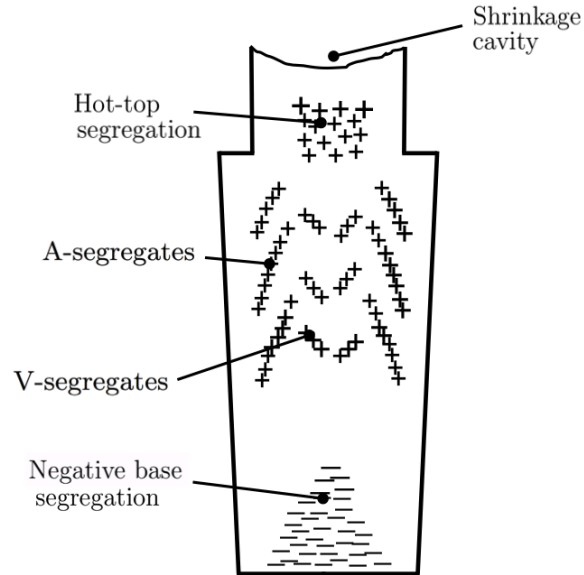


Figure 1: Schematic of the different types of macrosegregation typically found in large steel ingots. Positive segregation is denoted by + symbols (regions enriched in solute) and negative by - (regions depleted). A similar figure can be found in [8]. For further details of the mechanisms of macrosegregation that lead to such features, see reference [7].

Table 1: Composition (wt%) of the steel ingot investigated.

C	Si	Mn	P	S	Cr	Mo
0.79	0.80	0.26	0.007	0.005	4.88	0.33
Ni	V	Al	Cu	Sn	H	
0.22	0.005	0.008	0.08	0.009	2 ppm	

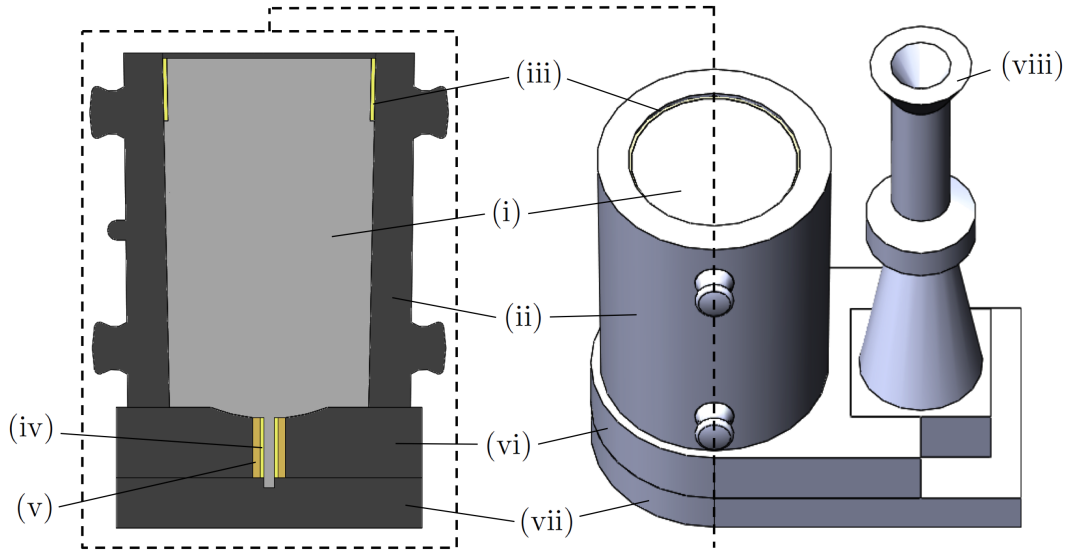


Figure 2: CAD drawings of the casting setup. Each component is described in Table 2.

Table 2: Casting assembly: descriptions and materials.

Label	Description	Material
(i)	Ingot	Steel
(ii)	Mould	Gray cast Iron
(iii)	Insulating tiles	Ceramic
(iv)	Hollow-ware	Ceramic
(v)	Packing sand	Silica (mostly)
(vi)	Cover plate	Gray cast Iron
(vii)	Base plate	Gray cast Iron
(viii)	Trumpet for pouring	Gray cast Iron

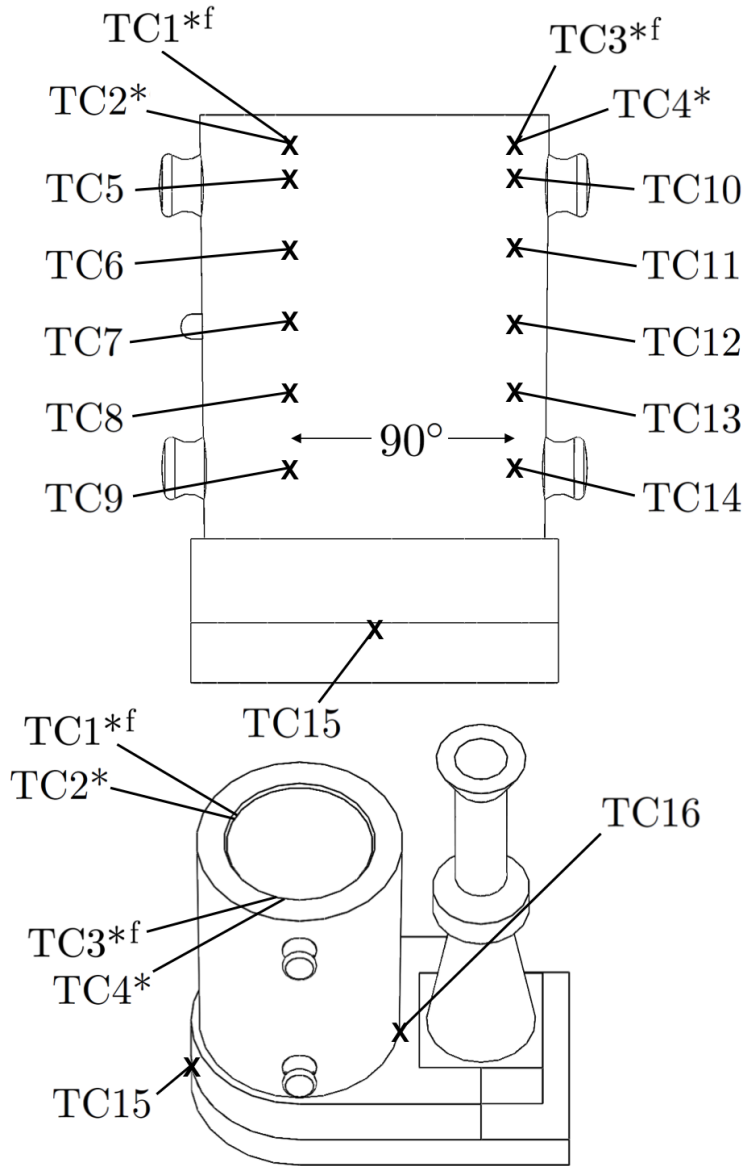


Figure 3: Placement of thermocouples on casting assembly. Thermocouples placed in the top of the mould between the mould and insulating tiles are labelled with superscript '\*'. TC1 and TC3 were held in place by friction (labelled with superscript 'f'), whilst the remaining thermocouples were cemented in position.

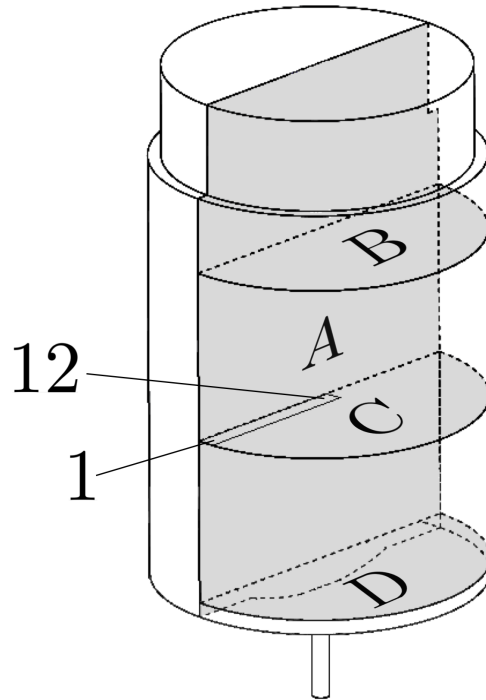


Figure 4: Schematic of ingot sectioning to reveal four faces, A-D. Also labelled is the radial strip in Face C, which was used for microstructural examination. Flutes on the outside have been removed.

Table 3: The stress-relief heat treatment used for the ingot.

Stage details	Duration /min
1. Equalisation at 400 °C	900
2. Heat 400 °C to 650 °C @ 20 °C h <sup>-1</sup>	750
3. Hold at 650 °C	900
4. Cool 650 °C to 600 °C @ 6 °C h <sup>-1</sup>	500
5. Cool 600 °C to 500 °C @ 8 °C h <sup>-1</sup>	750
6. Cool 500 °C to 400 °C @ 10 °C h <sup>-1</sup>	600
7. Cool 400 °C to 240 °C @ 12 °C h <sup>-1</sup>	800
8. Cooled in furnace (off) to room temperature	-

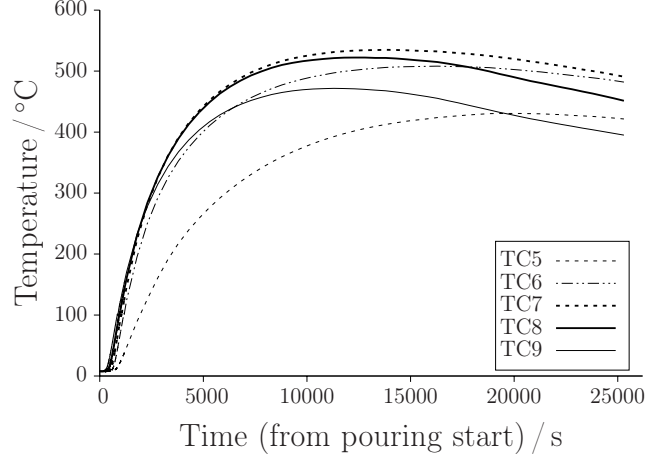


Figure 5: The thermocouple temperature readings for TC5-9.

Table 4: Estimations of the expansion of the mould and ingot, and the shrinkage gap magnitude in the cold state and shortly after stripping (both solid-state). The positions refer to those indicated in Fig. 7. The dimensions referred to are the ingot diameter (for the ingot) and the inside diameter of the mould (for the mould). The shrinkage gaps are given as a percentage of the inside diameter of the mould at the relevant temperature.

Position	Expansion of Ingot ( $\approx 15^\circ\text{C}$ - Stripping T)	Expansion of Mould ( $\approx 15^\circ\text{C}$ - $\approx 470^\circ\text{C}$ )
1	$0.44 \pm 0.06$ %	$0.44 \pm 0.05$ %
2	$0.57 \pm 0.05$ %	$0.63 \pm 0.12$ %
3	$0.68 \pm 0.07$ %	$0.47 \pm 0.12$ %
Position	Cold Shrinkage Gap (at $\approx 15^\circ\text{C}$ )	Hot Shrinkage Gap (shortly after stripping)
1	$1.19 \pm 0.03$ %	$1.96 \pm 0.20$ %
2	$1.20 \pm 0.05$ %	$1.96 \pm 0.13$ %
3	$1.27 \pm 0.06$ %	$1.70 \pm 0.19$ %

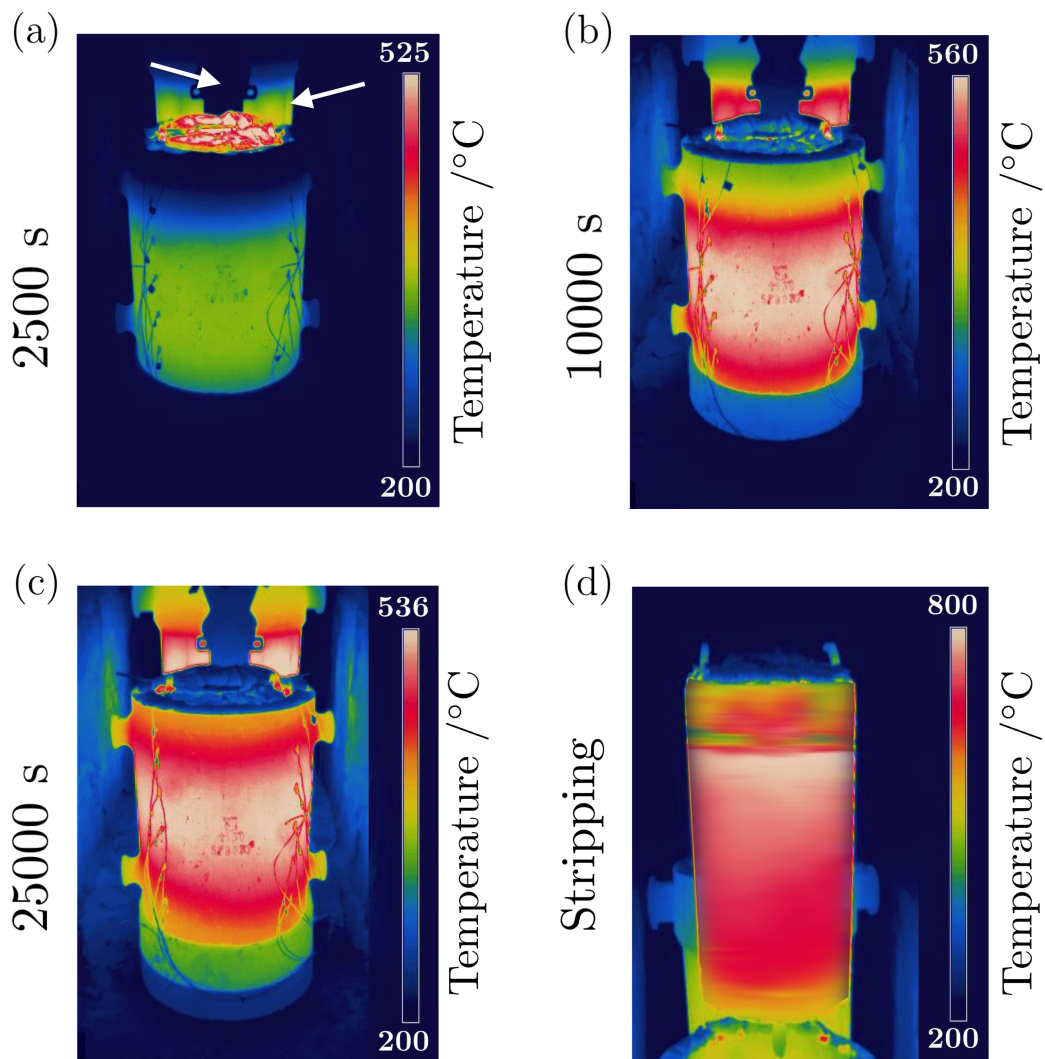


Figure 6: Thermal images of ingot mould at 2500, 10000, 25000 seconds (a-c), and the ingot immediately following stripping (d). The image in (d) has been doctored to blur the outer profile of the ingot (which was fluted) in the horizontal direction.

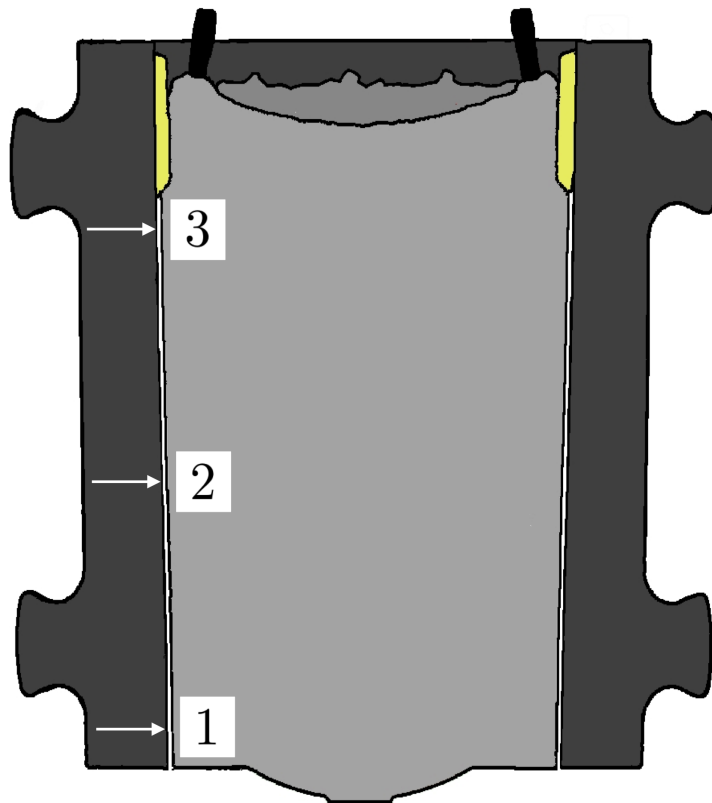


Figure 7: An illustration of the as-cast ingot sitting inside the mould, created using laser-measured dimensional data. Both ingot and mould are in the cold state (room temperature,  $\approx 15^\circ\text{C}$ ). The positions 1-3 in Table 4 refer to the indicated points 1-3 in this figure, for both mould and ingot.

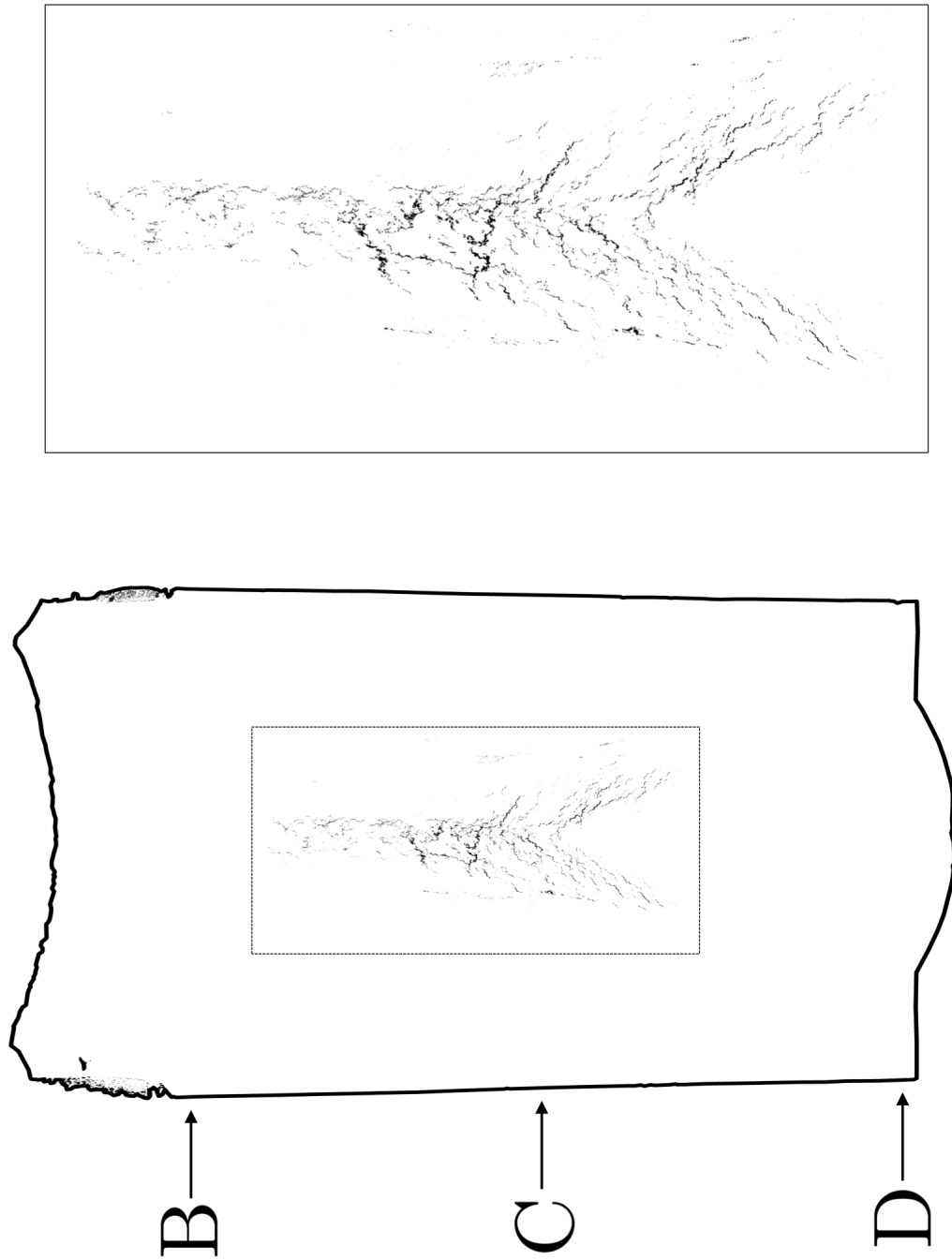


Figure 8: The porosity present in Face A, with the heights of Faces B-D indicated.

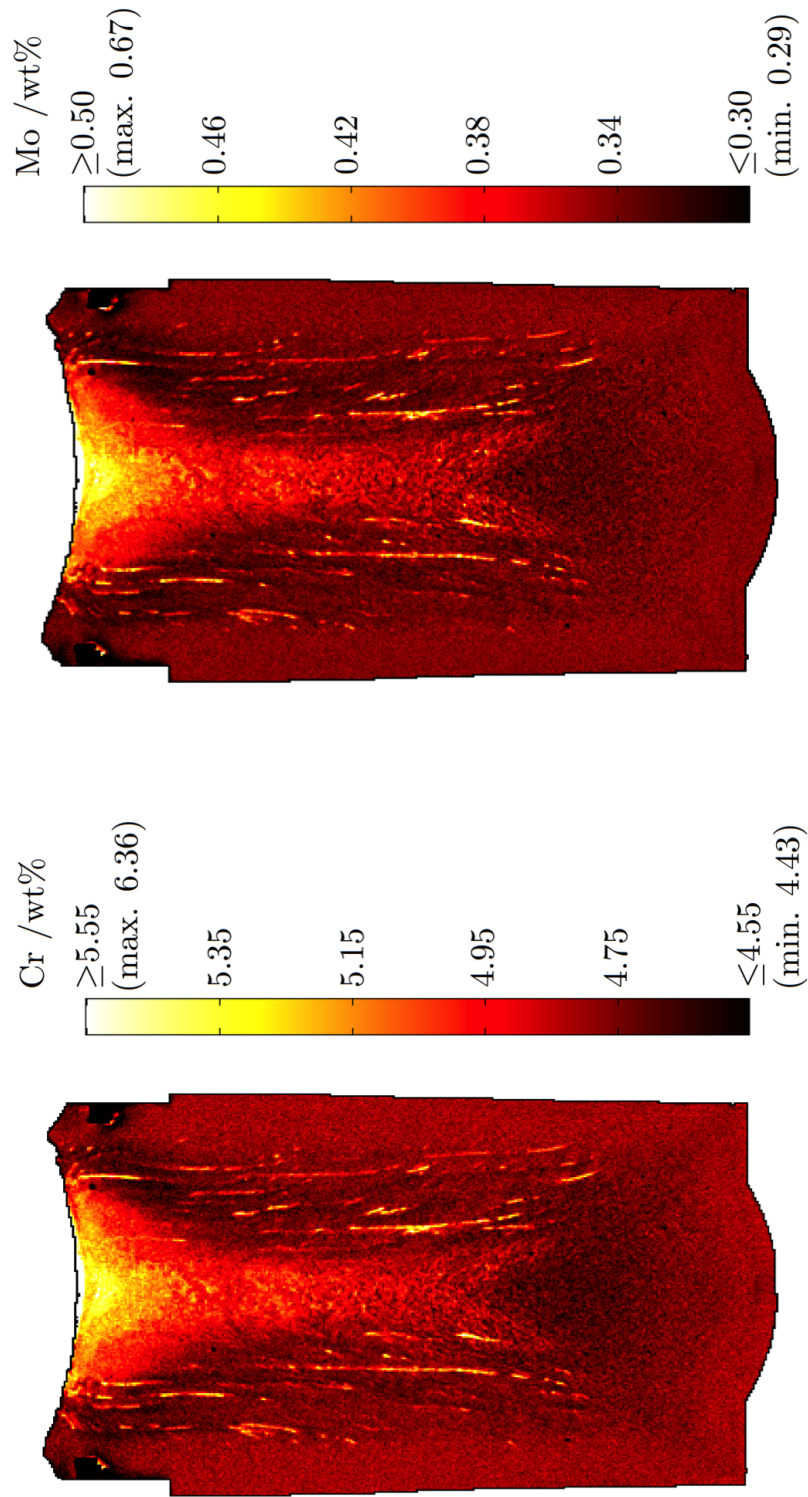


Figure 9: XRF maps for Cr and Mo on Face A.

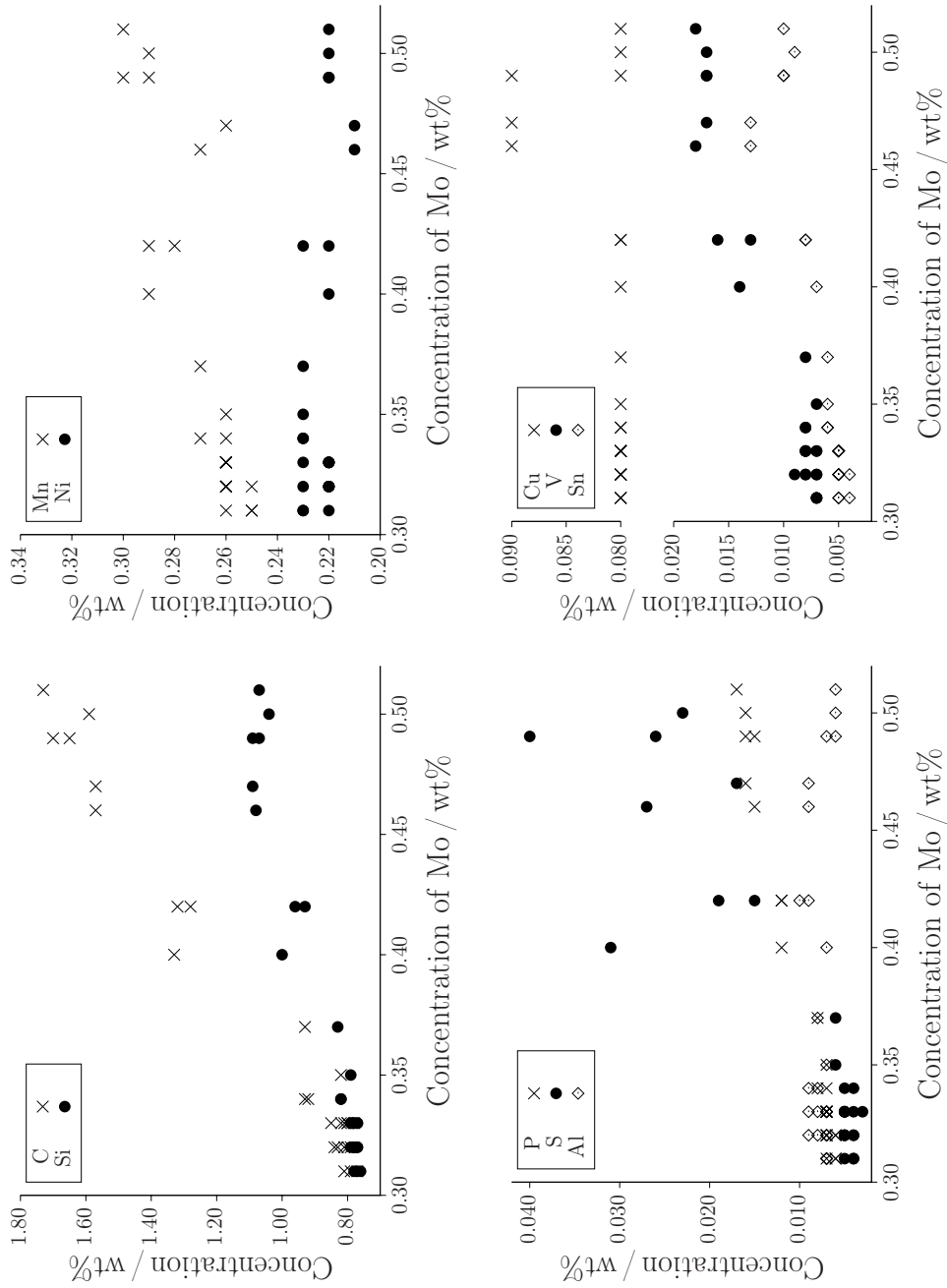


Figure 10: Concentrations of all species vs Mo, as measured using OES. Note the split axes in the plot for Cu, V and Sn.

Table 5: Approximate variations in secondary dendrite-arm spacings along the radial strip taken from Face C. Measurements were made at near the centre of each sample on multiple dendrite fragments where the arm spacings could be readily identified.

Position	Spacing / $\mu\text{m}$	Position	Spacing / $\mu\text{m}$
1	$102 \pm 17$	7	$332 \pm 71$
2	$115 \pm 22$	8	$333 \pm 51$
3	$235 \pm 37$	9	$295 \pm 46$
4	$296 \pm 49$	10	$320 \pm 63$
5	$282 \pm 82$	11	$340 \pm 39$
6	$319 \pm 101$	12	$294 \pm 64$

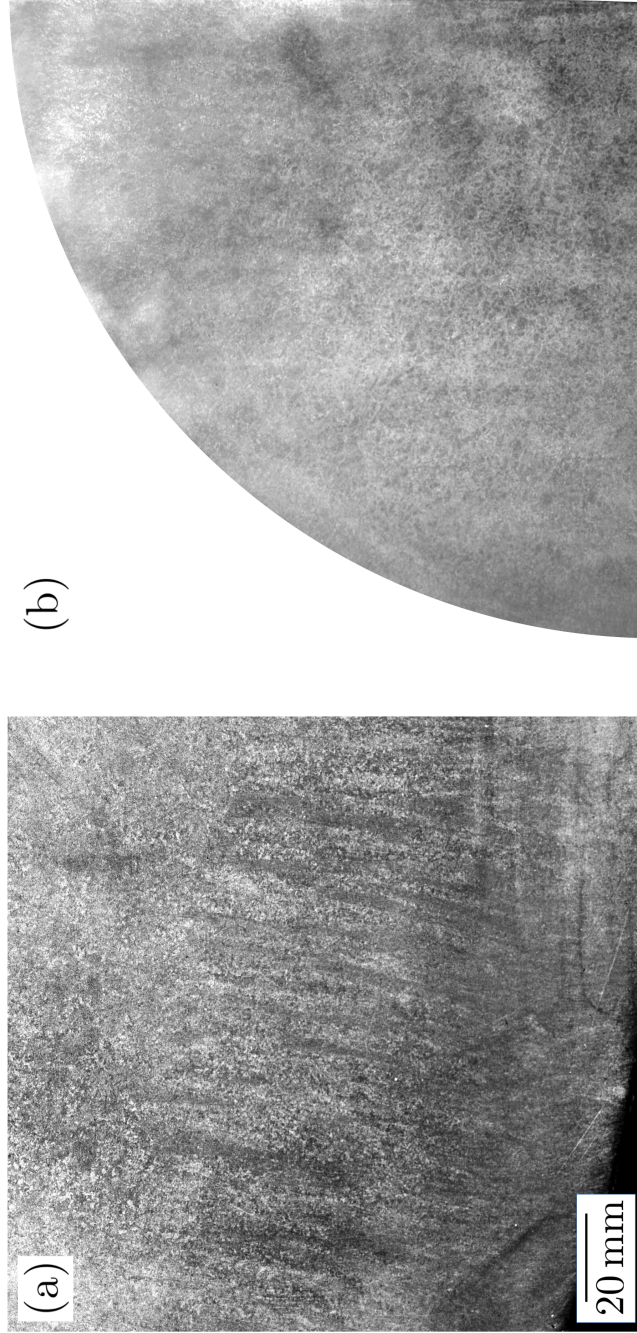


Figure 11: (a) Columnar dendritic grains found at the base of the ingot, which appear to have grown from the bottom edge for  $\approx 100$  mm. (b) Face B in the macroetched state. Note that vertical and circumferential streaks are associated with de-smutting and lacquering, not any structural features. Flutes have been removed from the outside edge of this face.

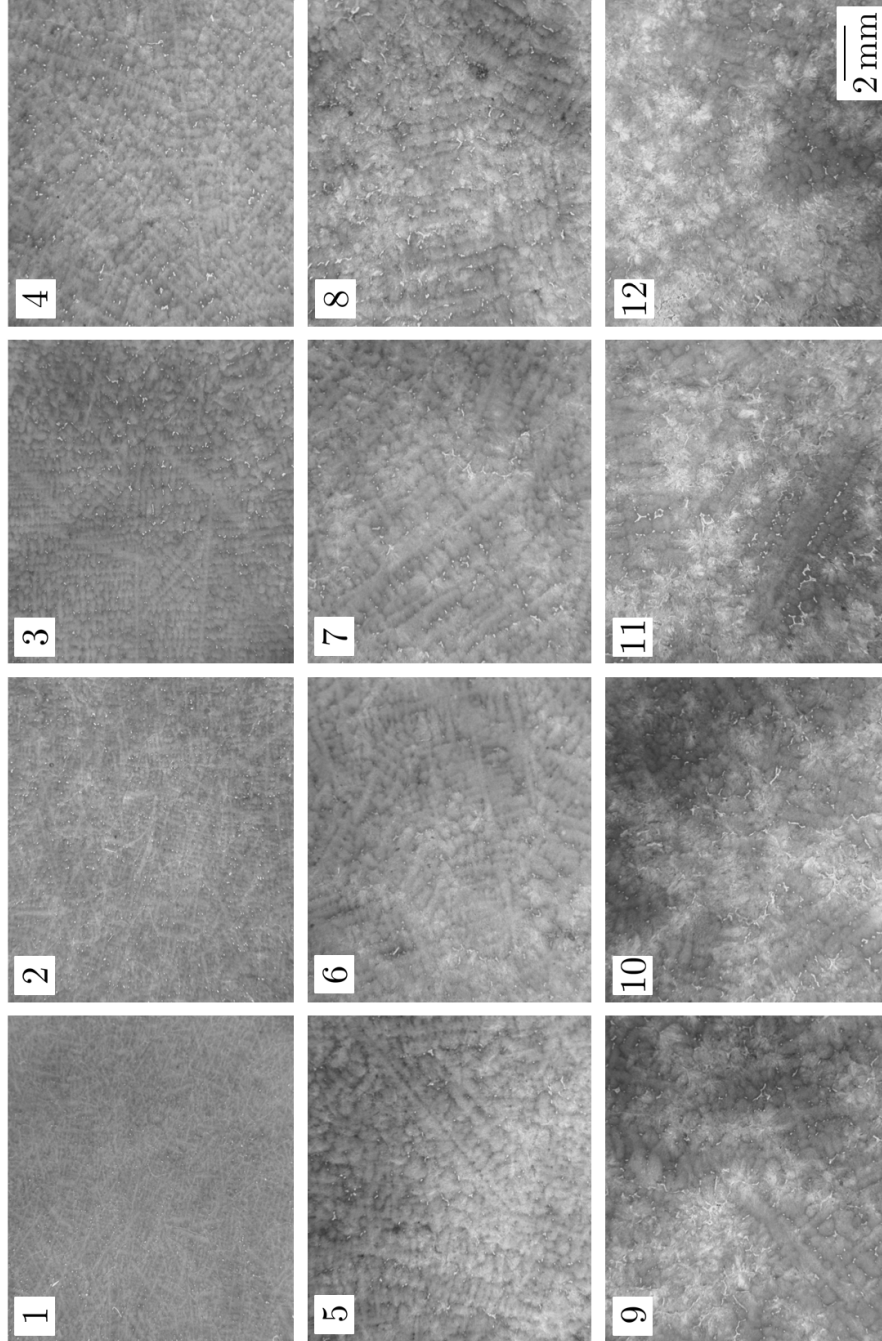


Figure 12: The variation in dendritic structure of the ingot along a radial section of Face C, viewing along the axial direction. Sample 1 was positioned at the outer edge of the ingot and Sample 12 directly adjacent to the centre, Fig. 4. All micrographs are shown in the same orientation, with the radial direction running horizontally, and the ingot centre on the right.

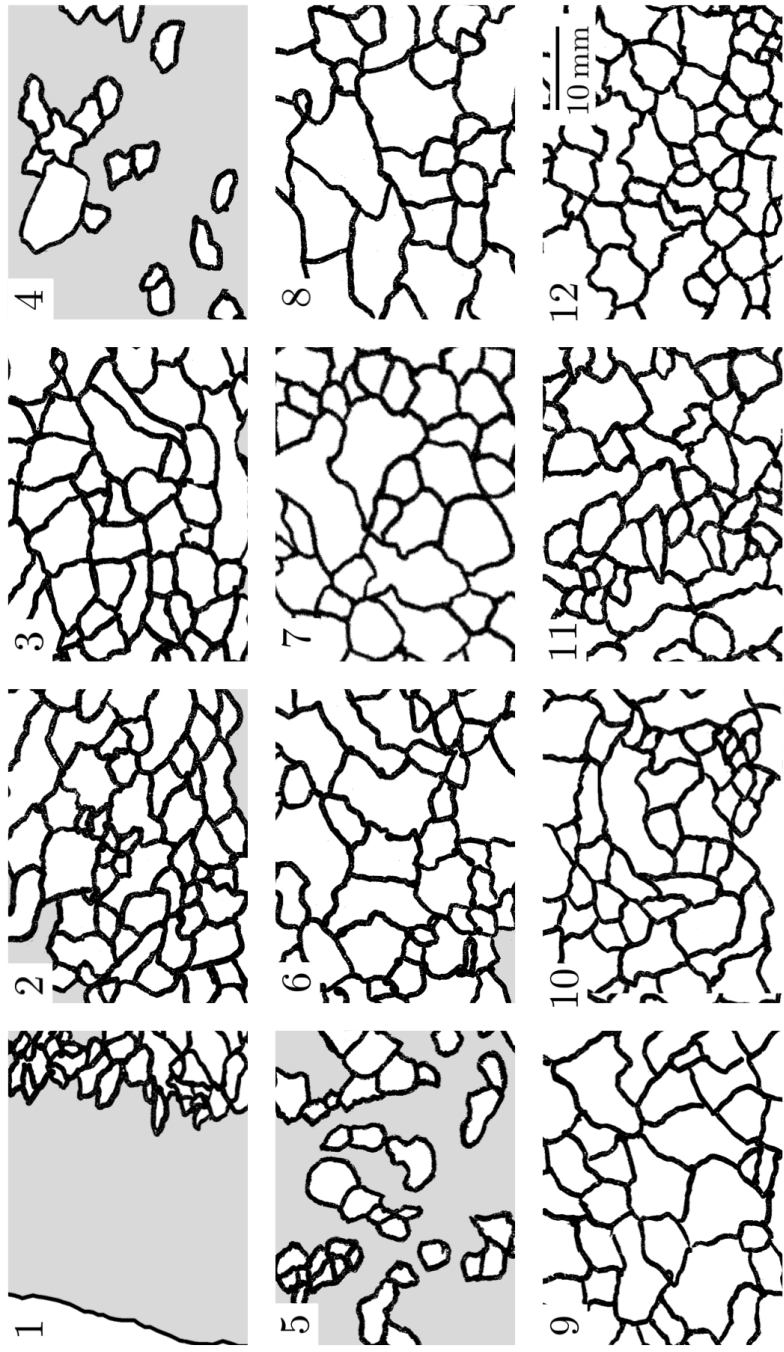


Figure 13: The grain structure of the ingot along a radial section of Face C, viewing along the axial direction. Grains were identified by overetching and outlining by hand; areas where this could not be achieved are shaded grey. All images are shown in the same orientation, with the radial direction running horizontally, and the ingot centre on the right.

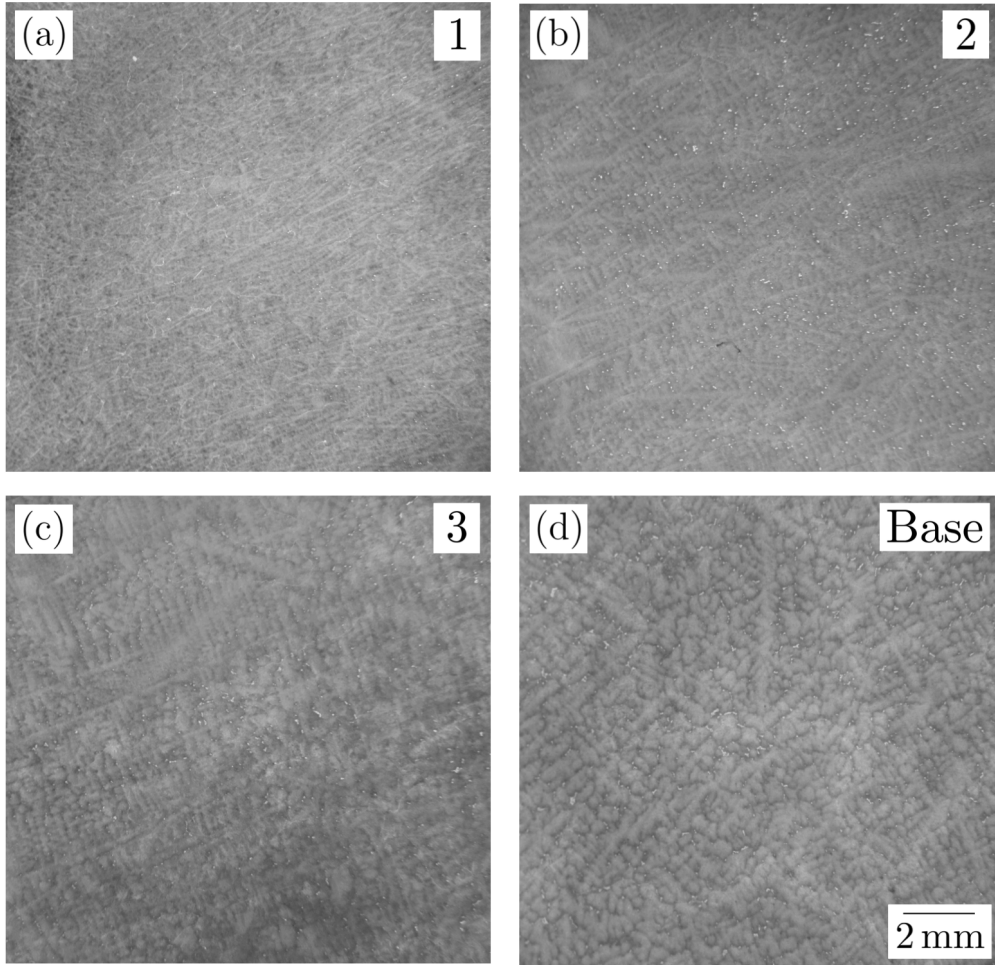


Figure 14: (a)-(c) The columnar dendrites in Samples 1-3, respectively, when viewing tangentially. They are angled away from the horizontal, towards the top of the ingot. Note that in (c) the beginning of a transition to a near-equiaxed morphology is observed. (d) The dendritic structure in the negatively-segregated cone at the base of the ingot.

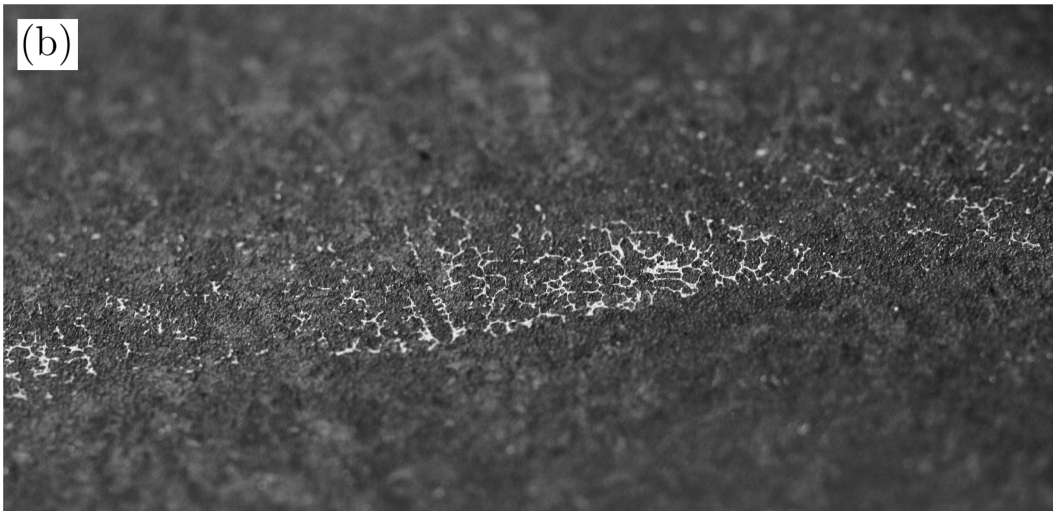


Figure 15: (a) A-segregate strings, present towards the bottom of the ingot. (b) A close-up image of the internal structure of a string. Both (a) and (b) were taken at a non-perpendicular angle to the surface of Face A. The channels were  $\approx 5$  mm in diameter.

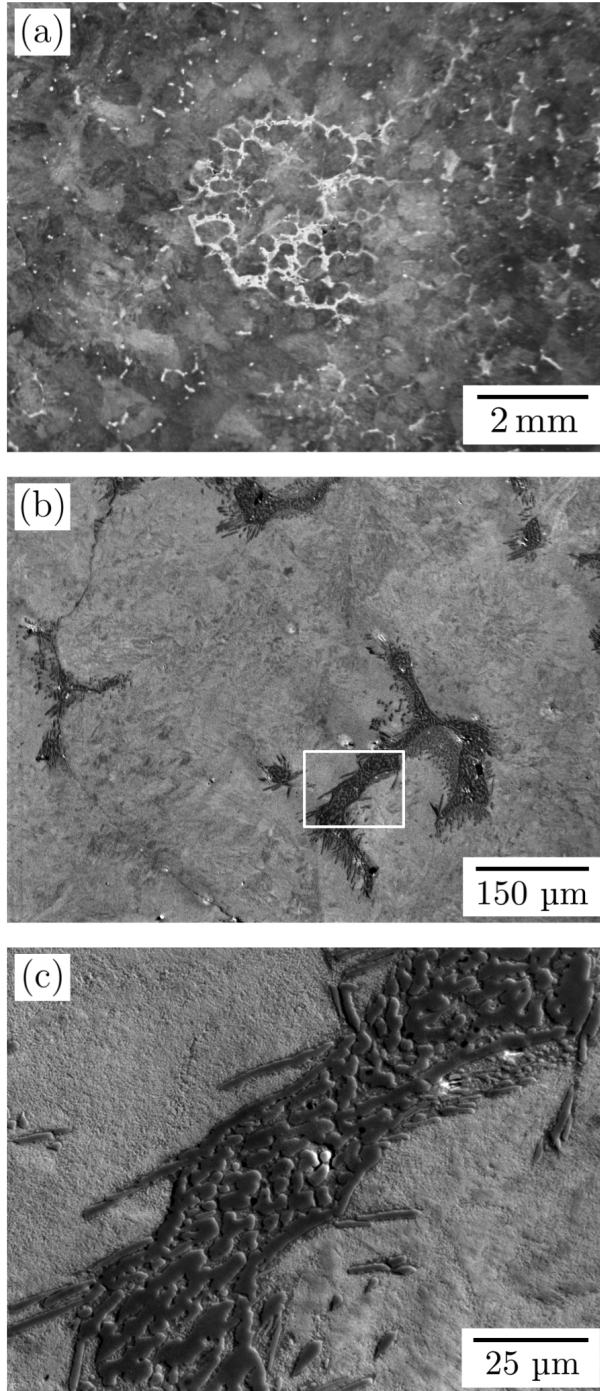


Figure 16: (a) The fine structure of an A-segregate channel, viewed axially in Sample 5. (b)-(c) Secondary-electron images of the interdendritic 'silvery' phase that is most prominent in A-segregates - the area in (c) is boxed in (b).

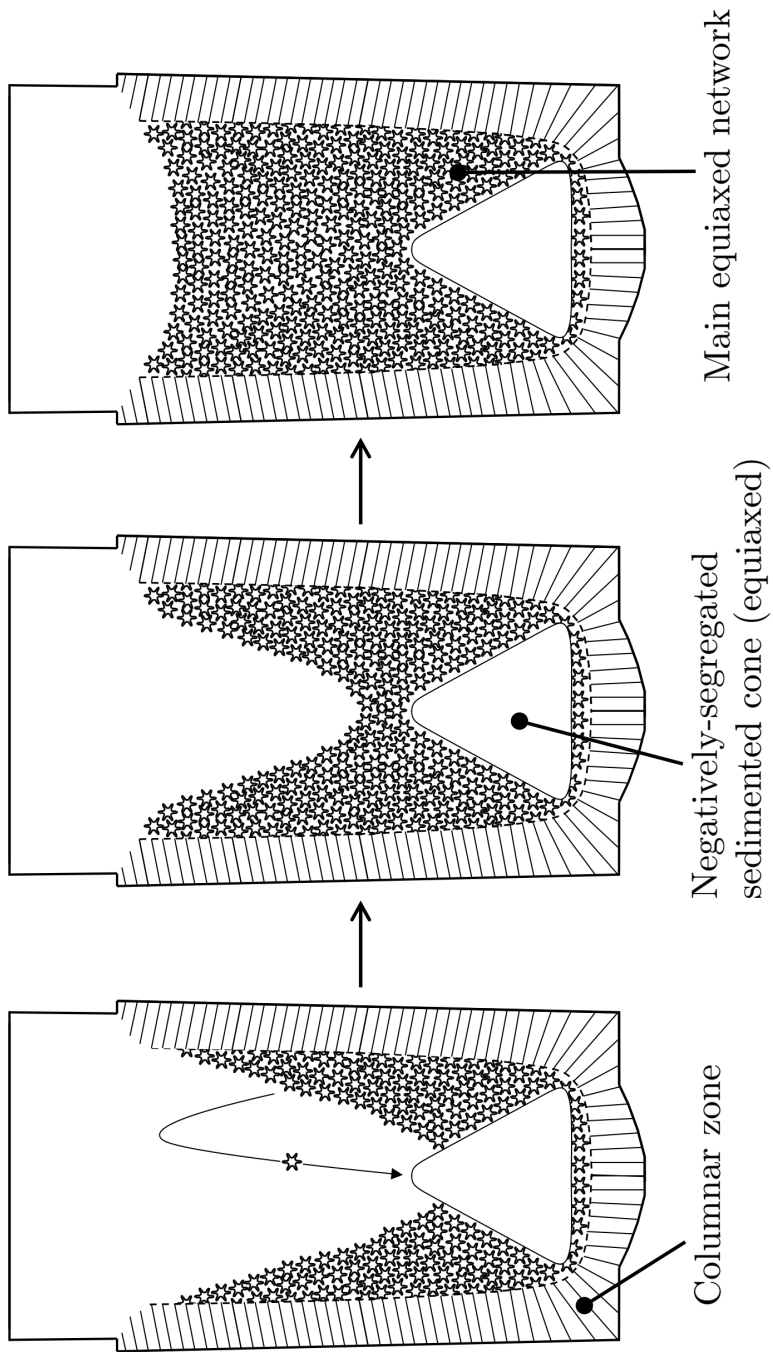


Figure 17: Schematic of a possible route for development of grain structure within the ingot. Note that the sizes of the zones, and the grains they contain, are not to scale. The negatively-segregated cone will also have been comprised of equiaxed grains, but these are not shown. A-segregates are also not shown.

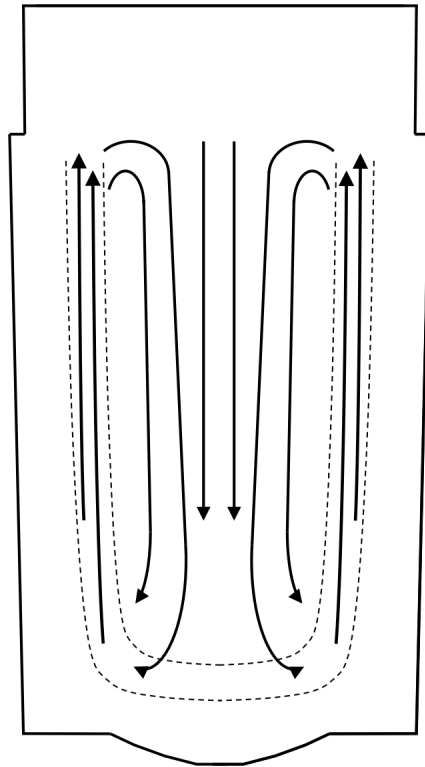


Figure 18: Schematic of possible fluid flow pattern in the ingot. Flow in the mushy zone (bounded by dashed lines) is strong, upwards, and primarily through channels (A-segregates). It is less-strong and generally downwards in the bulk zone. Note that this is exactly opposite to what might be expected from purely thermally-driven flows.

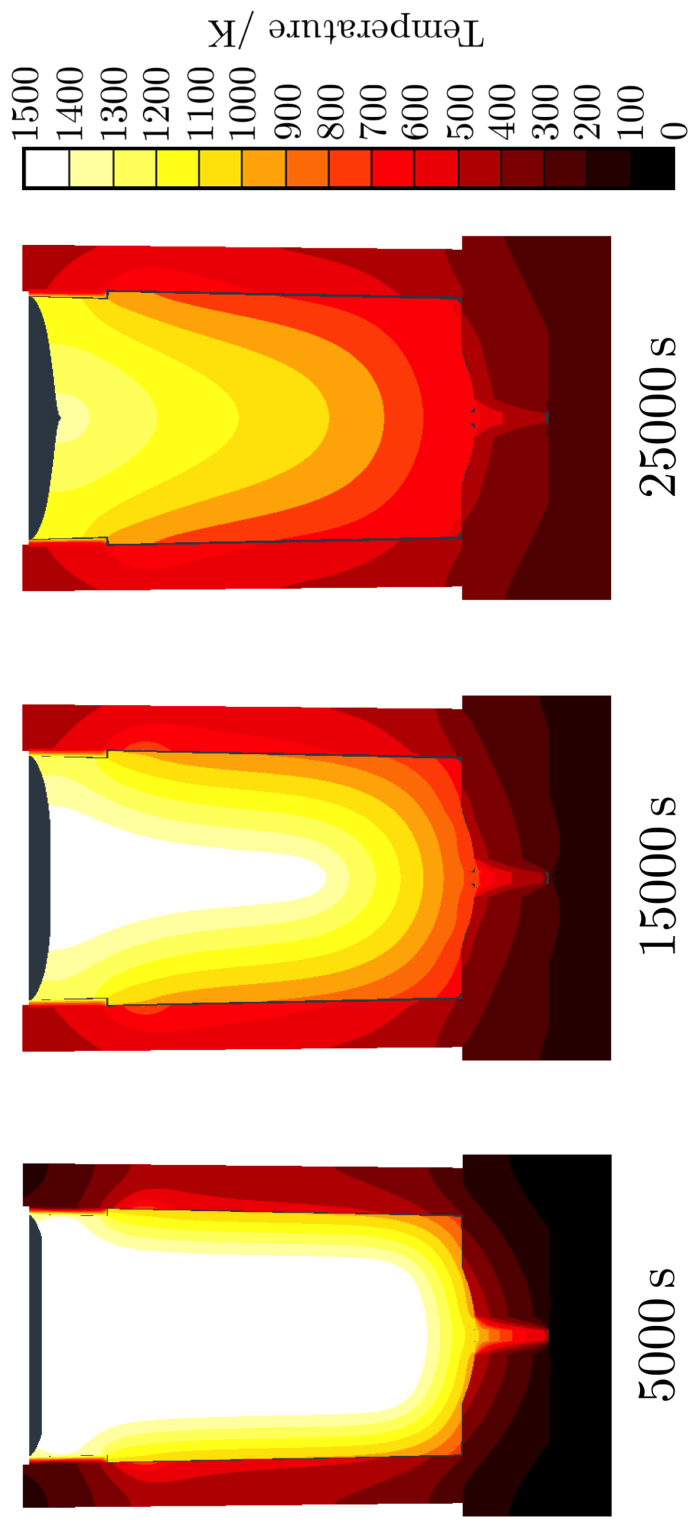
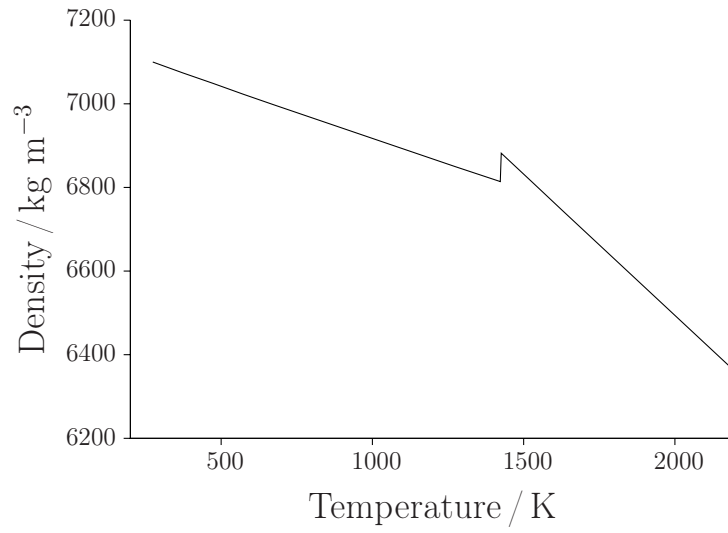
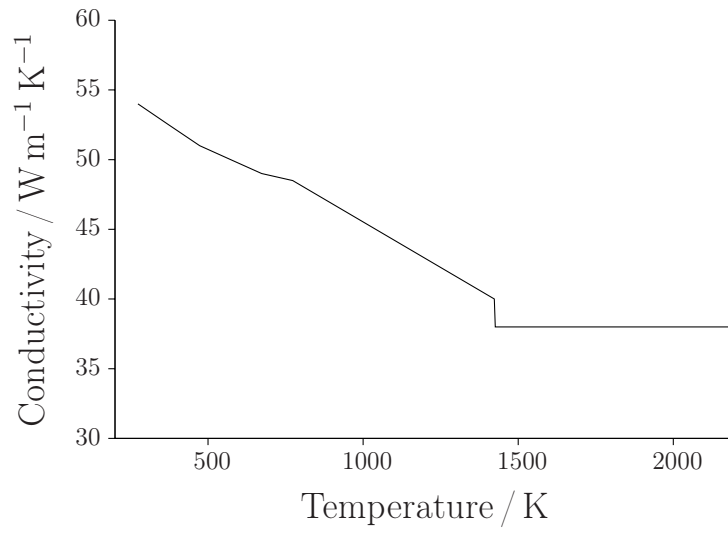
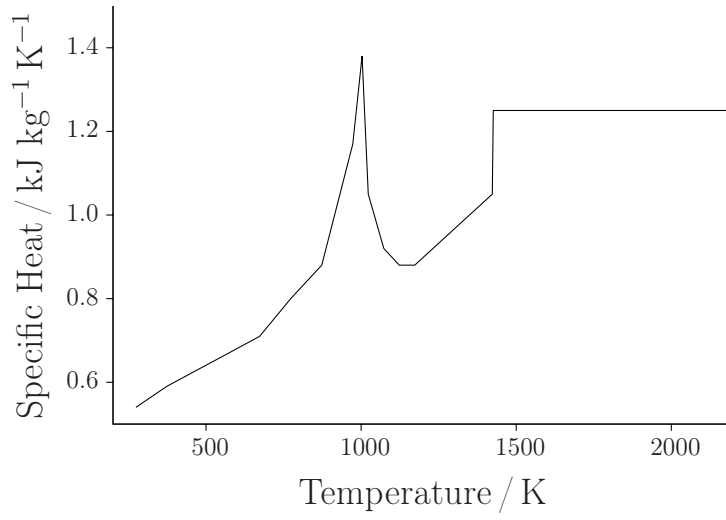


Figure 19: Isotherm pattern in the ingot and mould at various stages of solidification, as predicted using a finite-element model that accounted for the formation of a shrinkage gap, but did not account for fluid flow. For details see reference [24].

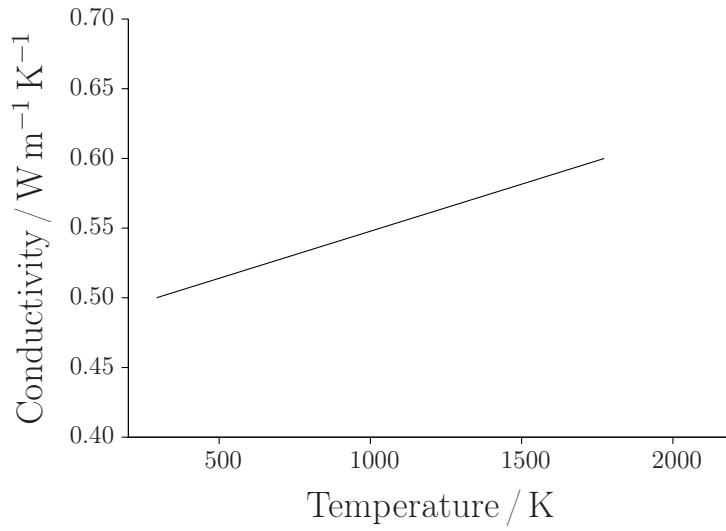
# Appendix 1

## Gray Cast Iron Properties





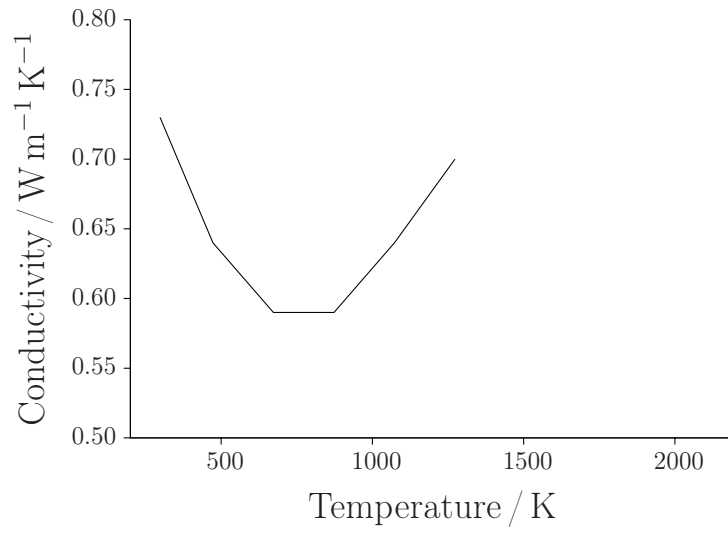
### Ceramic Properties



**Density** =  $1350 \text{ kg m}^{-3}$

**Specific Heat** =  $1.0 \text{ kJ kg}^{-1} \text{K}^{-1}$

## Sand Properties



Density =  $1520 \text{ kg m}^{-3}$

